
# Silica-embedded Gold Nanoparticles Analyzed by Atom Probe Tomography

# Silica-embedded Gold Nanoparticles Analyzed by Atom Probe Tomography

Gustav Eriksson, Mats Hulander, Mattias Thuvander, Martin Andersson

*Microscopy and Microanalysis*, 2024, **00**, 1–11
https://doi.org/10.1093/mam/ozae024
Advance access publication 25 March 2024
**Original Article**

Microscopy AND Microanalysis

# Silica-embedded Gold Nanoparticles Analyzed by Atom Probe Tomography

**Gustav Eriksson**[1], **Mats Hulander**[1], **Mattias Thuvander**[2], **and Martin Andersson**[1,*]

[1]*Department of Chemistry and Chemical Engineering, Chalmers University of Technology, Kemigården 4, SE-41296 Gothenburg, Sweden*
[2]*Department of Physics, Chalmers University of Technology, Kemigården 1, SE-41296 Gothenburg, Sweden*

***Corresponding author:** Martin Andersson, E-mail: martin.andersson@chalmers.se

## Abstract

Nanoparticles are utilized in a multitude of applications due to their unique properties. Consequently, characterization of nanoparticles is crucial, and various methods have been employed in these pursuits. One such method is Atom Probe Tomography (APT). However, existing sample preparation techniques for APT generally involve embedding of the nanoparticles in a matrix different from their environment in solutions or at solid–liquid interfaces. In this work, we demonstrate a methodology based on silica embedding and explore how it can be utilized to form a matrix for nanoparticles suitable for APT analysis. Through chemisorption to a surface, gold nanoparticles were densely packed, ensuring a high probability of encountering at least one particle in the APT analyses. The nanoparticle-covered surface was embedded in a silica film, replacing the water and thus making this method suitable for studying nanoparticles in their hydrated state. The nanoparticle's silver content and its distribution, originating from the nanoparticle synthesis, could be identified in the APT analysis. Sodium clusters, possibly originating from the sodium citrate used to stabilize the particles in solution, were observed on the nanoparticle surfaces. This indicates the potential for silica embedding to be used for studying ligands on nanoparticles in their hydrated state.

**Key words:** atom probe tomography, gold nanoparticles, silica embedding, stabilizing ligands

## Graphical Abstract

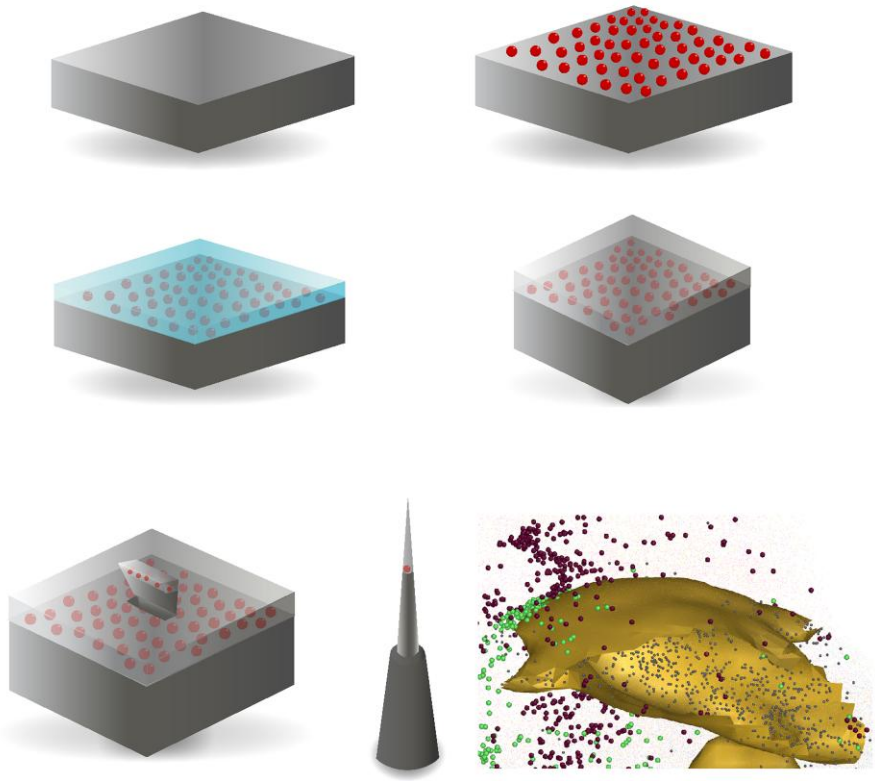

**Received:** October 31, 2023. **Revised:** February 9, 2024. **Accepted:** March 2, 2024

## Introduction

Nanoparticles, due to their versatility, have dramatically increased in usage for various applications over recent decades. Such applications include, but are not limited to, catalysis, biosensing, and energy conversion (De et al., 2008; Joo et al., 2009; Stark et al., 2015). Numerous protocols have been developed for the synthesis of nanoparticles, and their shape as well as their size can be controlled to a high degree (Rajput, 2015). Both top-down and bottom-up procedures are common pathways to synthesize nanoparticles. Employing colloidal synthesis, nanoparticles have successfully been shaped into various forms such as spherical, concave cubes, octahedral, rhombic dodecahedra, and ditetragonal prisms (Personick et al., 2011). The shape of such metallic nanoparticles, often made from gold, can be controlled by the addition of other metal cations, especially silver, during synthesis (Personick et al., 2011). However, integrating other metals into nanoparticles can alter their properties and functionalities in applications like catalysis and biosensing by modifying the chemical nature of the surface.

Considering the widespread use of nanoparticles, there is a high demand for thorough characterization. Various techniques are utilized to give information regarding their shape, composition, surface area, morphology, etc. (Ealias & Saravanakumar, 2017). All these techniques are valuable, as nanoparticle properties can be accurately fine-tuned and are intrinsically linked to their function. Detailed information on surface properties and bulk chemistry of nanoparticles, particularly when the nanoparticles consist of more than one element or those with several phases or stabilizing ligands, can be of interest to correlate nanoparticle formation, structure, properties, and function. However, obtaining high-quality information may be challenging due to their small size and heterogeneous nature. Transmission Electron Microscopy (TEM) has been used to study the distribution of constituent elements in gold–silver alloyed nanoparticles with Energy Dispersive X-ray Spectrometry (EDX) (Mahl et al., 2012; Rioux & Meunier, 2015). This illustrates gold enrichment closer to the core of seeded growth synthesized gold–silver alloy nanoparticles. Detailed analysis, however, can be challenging due to the limited sensitivity and resolution of EDX (Reddy et al., 2020). In particular, it is time consuming to obtain data with high spatial resolution and sufficient signal-to-noise ratio, which limits the technique for electron beam sensitive materials (Mourdikoudis et al., 2018). Examples of such sensitive materials can be the stabilizing ligands often used on nanoparticles. Here, Atom Probe Tomography (APT) can fill a niche where it complements other characterization techniques with its high mass resolving power, ppm sensitivity across the entire periodic table, and sub-nanometer resolution (Gault et al., 2021). It is highly suitable for use when investigating low concentration solutes in nanoparticles with high sensitivity and spatial resolution.

Historically, APT has mainly been used to study metallic materials and their alloys, while the development of the laser-assisted atom probe and the utilization of focused-ion-beam (FIB) instruments for site-specific sample preparation have broadened its usage to additional materials. Several sample preparation methods, each with distinct advantages and limitations regarding specimen survivability, output data quality, and the probability of locating the nanoparticles within the analyzed volume, have been explored for nanoparticle analysis (Felfer et al., 2015). For example, APT has been used to study the internal structure of core–shell particles (Felfer et al., 2014; Kim et al., 2020) and ligands on nanoparticles (Qiu et al., 2020; Jang et al., 2021).

When examining new materials, especially nonbulk materials such as nanoparticles, challenges always arise concerning method development for sample preparation. Several protocols have been assessed where a surface covered with nanoparticles has been embedded using sputter coating or atomic layer deposition (ALD). Sputter coating has been shown to cause voids in the structure, which are known to cause issues when attempting to analyze the material with APT (Wang et al., 2020; Mosiman et al., 2021). Consequently, alternative methods like ALD, electrodeposition or even liquid metal melts have been employed to embed nanoparticles on surfaces (Kim et al., 2021). Investigating the liquid–solid interface is of interest in numerous materials science applications, and an additional challenge with the established methods is that nanoparticles formed and used in an aqueous dispersion will be forced into a metal matrix for analysis, potentially modifying their surface. The aforementioned methods can also potentially alter the structure of the nanoparticles; for example, due to high temperatures during the preparation procedures. Nonetheless, a persisting challenge remains on how to increase the probability of encountering a nanoparticle within the analyzed volume.

In this paper, we present a method for nanoparticle analysis using APT. Nanoparticles were formed in dispersion using a seed–growth protocol and deposited on a flat substrate using a linker. This provided discrete particles with a tunable distance, and they were subsequently embedded by spin-coating a silica sol–gel. This provides a matrix that can preserve the surface and ligand nature on the particles in their hydrated state without alterations induced by the embedding process. Replacing water with silica has demonstrated to enable APT analysis of proteins while retaining their structure (Sundell et al., 2019). Simulations have also shown that this process can retain the structure of such complex organic molecules in the hydrated state (Novi Inverardi et al., 2023). Previous work has shown that this type of material can be studied using APT using conventional sample preparation methods (Sundell et al., 2019) without any need for cryogenic equipment or vacuum transfer. Furthermore, this method gives a relatively high throughput by providing a high likelihood of finding nanoparticles in every APT specimen.

## Materials and Methods

### Nanoparticle Formation

Gold nanospheres were formed according to a conventional seed–growth protocol (Goia & Matijević, 1998; Park & Park, 2008), schematically illustrated in Figure 1. Initially, a gold seed solution was prepared by adding 100 mL of a 1.0 mM $HAuCl_3$ solution to 100 mL Milli-Q water and heated to 100°C while stirring. Upon reaching the boiling temperature, 10 mL of 38 mM sodium citrate was added, and the solution was boiled for 80 min followed by cooling to room temperature. Subsequently, the seed–growth solution was prepared by adding 2 mL of 20 mM $HAuCl_3$ into 85 mL milli-Q water while stirring, followed by the addition of 200 µL of 10 mM $AgNO_3$ in order to ensure a spherical shape of the final nanoparticles. All solutions containing $AgNO_3$ were wrapped in aluminum foil to protect them from light. To grow the seeds into the desired final nanoparticle size, 7.5 mL of the seed solution was added to the growth solution. The particle growth was then controlled by

adding 15 mL of 5.3 mM ascorbic acid at a rate of 0.6 mL/min. The final solution was left under stirring overnight.

## Material Assembly

The samples were prepared by adhering gold nanoparticles to silicon wafers that were precovered by a 10 nm chromium film, as acquired from Substrata, Ångström Engineering. Prior to starting the work, the wafers underwent a heat-treatment at 600°C for 2 h, which aimed to augment the adhesion of chromium to the silicon substrate. The wafers were then cleaned by ultrasonication in isopropanol followed by ethanol for 30 min, respectively, and then treated in a $UV/O_3$ oven for 1.5 h post washing with Milli-Q water and drying with $N_2$ (g). The wafers were then submerged in a 2% (3-mercaptopropyl) trimethoxysilane, $HS(CH_2)_3Si(OCH_3)_3$, commonly known as MPTMS, in toluene for 45 min to form a self-assembled thiol-terminated monolayer on the wafer surface. This was followed by sequential transfers into toluene, ethanol, and Milli-Q water. Alternate linkers were also evaluated, including (3-aminoproypyl) triethoxysilane (APTES), with less satisfactory results. The surface-modified wafers were submerged in gold nanoparticle dispersion for 1.5 h and subsequently transferred through Milli-Q water, ethanol and toluene before being dried. The surface coverage of nanoparticles was assessed using scanning electron microscopy (SEM) utilizing a LEO Ultra 55 instrument operating at 10 keV and collecting secondary electrons with the in-lens detector.

In a separate experiment, attempts were performed to attach proteins to the nanoparticles by adding thiol containing streptavidin, acquired from NanoCs Inc., at a concentration of 50 µg/mL in PBS buffer on the nanoparticle-modified surface for 3 h prior to silica embedding.

Embedding was performed by preparing a silica sol–gel solution according to a so-called water glass methodology, which has been successfully utilized in prior instances for preparing materials for APT analysis(Bhatia et al., 2000; Sundell et al., 2019). Specifically, a 28.7% sodium silicate solution, diluted to 1:3 by milli-Q water, was pH-adjusted to 6 by running it through an ion exchange column prepared by adding Dowex 50-W highly acidic cation exchanger mesh to a 5-mL syringe. A quantity of 75 µL of the pH-adjusted sol–gel solution was spin-coated on the surfaces at 1,750 × *g* and subsequently left to dry in an oven at 37°C.

The complete process of adhering gold nanoparticles onto the silicon wafers and embedding the modified surfaces in silica is schematically illustrated in Figure 2.

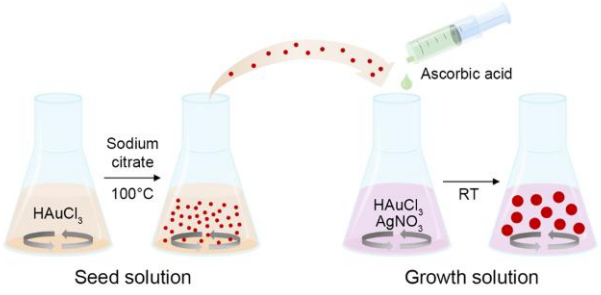


**Fig. 1.** Schematic overview of the gold nanoparticle seed–growth synthesis protocol. A gold seed solution is prepared by adding sodium citrate to a boiling $HAuCl_3$ solution. Larger gold nanospheres are obtained by adding seed particles to a solution containing $HAuCl_3$ and $AgNO_3$ followed by controlled addition of ascorbic acid.

## APT and TEM Specimen Preparation and Analysis

Specimens for APT (and TEM) were prepared according to standardized dual-beam FIB–SEM protocols (Thompson et al., 2007; Hernández-Saz et al., 2012). Prior to specimen preparation, an Au layer was deposited by sputter coating. A protective Pt-coating, with a thickness of 1.5 µm, was deposited on the region to be lifted out using the instrument's gas injection system. The area of interest was then isolated by Ga-ion milling at 5 nA followed by polishing at 1 nA before attachment to an Omniprobe micromanipulator by Pt-deposition. The TEM lift-out was attached by Pt-deposition to a copper half grid and gradually milled thinner using rectangular cleaning cross-section patterns starting at 0.5 nA and sequentially lower currents until the protective Pt-layer was almost removed and the sample was sufficiently thin at the region of interest.

The APT lift-out was placed in slices on silicon flat-top microposts (Cameca Scientific Instruments) and sharpened by annular milling starting at 1 nA and with stepwise reduced current as well as inner and outer diameter. After removal of the protective Pt-layer, the final milling was performed at 5 kV and 7 pA without an inner diameter. The APT lift-out procedure and final TEM lamella imaged during specimen preparation are shown in Supplementary Figures SI2 and SI3.

The TEM samples were analyzed in an FEI Titan operating at 300 kV in normal TEM mode. APT specimen analysis was executed using two distinct systems, an Imago LEAP 3000X HR system (Imago Scientific Instruments) in laser mode using a green laser ($\lambda = 532$ nm) and a LEAP 6000 XR system (Cameca Scientific Instruments) in laser mode using a deep-UV laser ($\lambda = 257.5$ nm). In the LEAP 3000X HR system, the pulse frequency was set at 100 kHz to avoid the time of flight of gold to be longer than the time between pulses, causing confusion in the mass spectrum. The pulse energy was kept at 0.2–0.3 nJ, sample temperature 55 K, while the average evaporation rate during the analysis was 0.002 ions per pulse. Data were reconstructed utilizing IVAS software version 3.6.8. (Cameca Scientific Instruments) following a standard voltage evolution-based protocol, applying varied reconstruction factors.

In the LEAP 6000 XR system, the pulse energy was set to 0.1 nJ, specimen temperature at 50 K, and the detection rate

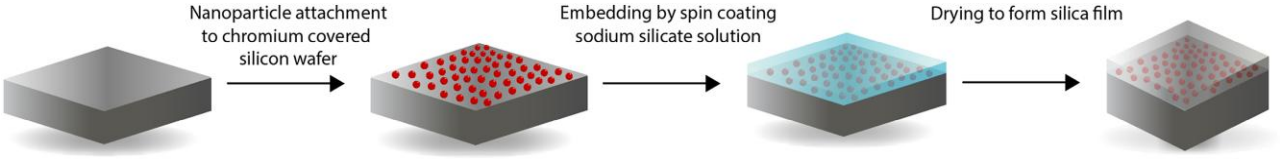


**Fig. 2.** Schematic overview of the gold nanoparticle embedding into silica. Nanoparticle-covered surfaces are consequently embedded in silica by spin-coating a sodium silicate solution, adjusted to neutral pH by running it through an ion exchange column. A silica film is formed by drying the material at 37°C.

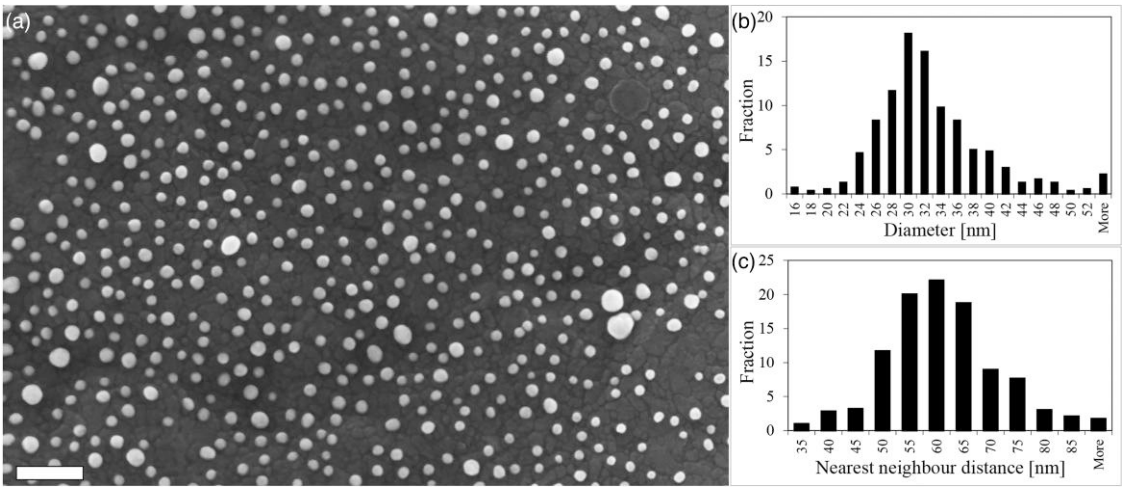


**Fig. 3.** (**a**) SEM micrograph showing a nanoparticle-modified substrate surface. The scale bar is 200 nm. (**b**) Distribution of the diameters of the 541 nanoparticles in (**a**). (**c**) Distribution of nearest neighbor distances (center–center) for the nanoparticles.

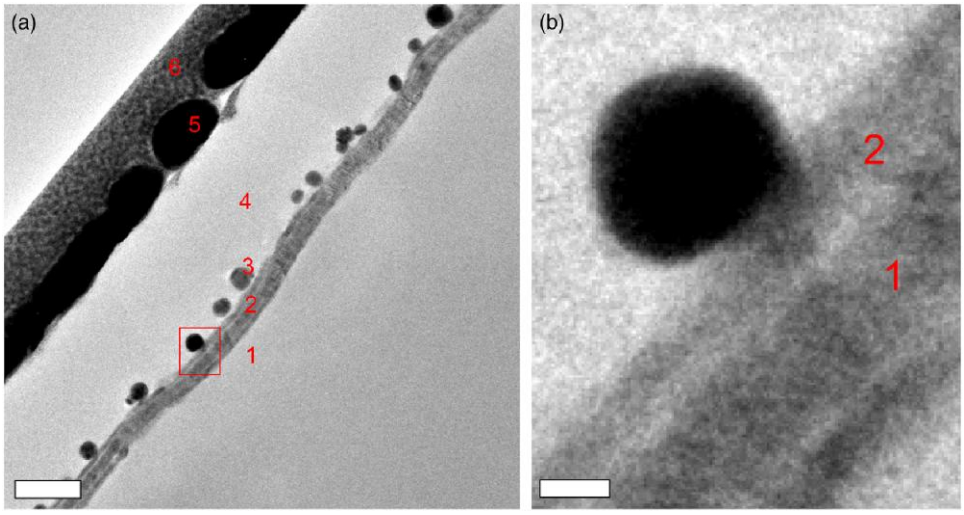


**Fig. 4.** (**a**) TEM micrograph showing an overview of gold nanoparticles embedded in a silica film. Labeled regions are (1) silicon substrate, (2) Chromium layer, (3) Gold nanoparticle, (4) Spin-coated silica film, (5) Sputter coated protective Au-layer, (6) GIS-deposited protective Pt-layer. The scale bar is 100 nm. (**b**) shows the region indicated by a box in (**a**) magnified. The effect of heat-treatment on the chromium layer is distinguishable. (1) shows the chromium layer, (2) shows the chromium oxide layer. The scale bar is 10 nm.

at 0.002 ions per pulse. The pulse frequency was varied depending on the voltage with the auto pulse rate control set to 250 Da, to ensure that the heavy ions were collected before the next pulse. Data obtained with this system were reconstructed using AP Suite version 6.2 software (Cameca Scientific Instruments) using a voltage evolution-based protocol.

## Results and Discussion

### *Nanoparticle Formation and Deposition*

The size distribution and surface coverage of gold nanoparticles after deposition on the substrate were assessed by SEM. The substrate's surface was evenly covered with nanoparticles, as seen in Figure 3. The rugged nature of the underlying surface is due to the heat-treatment prior to nanoparticle deposition, forming a chromia layer. This is not seen in the untreated samples, which rather displayed a smooth surface.

Image analysis was performed using the ImageJ software (National Institutes of Health) to determine the nanoparticle size distribution and surface coverage and the results can be found in Figures 3b and 3c, respectively. The particles were found to have a size distribution with an average diameter of $32 \pm 8$ nm based on the 541 nanoparticles in Figure 3a. The average nearest neighbor distance was measured to $58 \pm 11$ nm, which is sufficiently short to achieve a satisfactory probability of finding a particle in a prepared APT specimen. It should be noted that the surface coverage is a result of the electrostatic interactions between the nanoparticles, so while the particles in the present study could be closely packed, alternative particles may not, potentially requiring a buffer solution adjustment to mitigate particle repulsion and secure optimal packing. Additionally, different substrate surface modifications might also prove to be more suitable for other nanoparticles.

### *Nanoparticle Embedding*

The final material, featuring nanoparticles embedded within a silica film, was analyzed using TEM (Fig. 4a). The silica film,

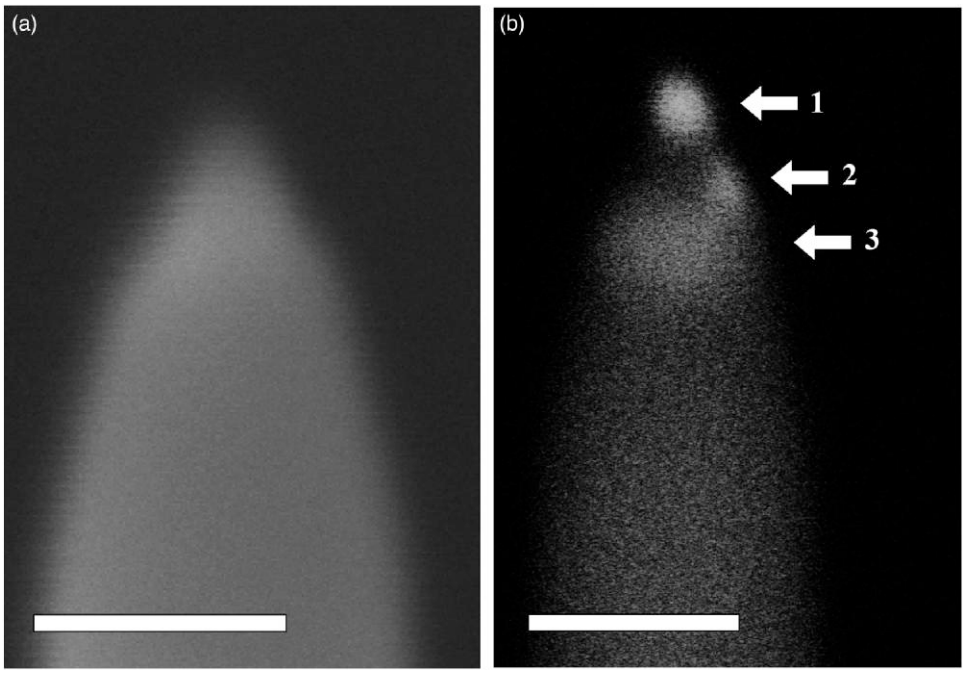


**Fig. 5.** SEM micrographs of a polished atom probe specimen. In (**a**), the specimen is imaged using secondary electrons. In (**b**), the specimen is imaged using backscattered electrons, where high Z regions appear brighter. Regions indicated with arrows are (1) protective Au-layer, (2) Au nanoparticle, (3) chromium and chromium oxide layer. The scale bars are 100 nm.

approximately 190 nm thick, provided a suitable region for the apex of the APT specimen following the final polishing of the tips, showing that the spin-coating provided a high degree of control to obtain a desired silica layer thickness by modulating the rotation speed and time. It should be noted that the silica layer thickness varied throughout the sample due to the spin-coating process, being thinnest in the center and progressively thicker toward the edges. The nanoparticles remained well separated, with a distance between them sufficiently short to ensure a high likelihood of encountering at least one in the final APT specimen. Furthermore, no obvious voids were observed around the nanoparticles or the underlying substrate. This shows that the spin-coating of the sol–gel solution, and subsequent drying, gives a dense film that fills all available space and is not susceptible to shadowing effects that may occur when depositing films by sputter coating. Higher magnification imaging using TEM reveals nano-porous structures of the silica; however, these did not seem to pose the same kind of problems as larger pore sizes when analyzing using APT, with respect to causing specimen fractures or artifacts in the data reconstruction (Miller et al., 2011).

The effects of the heat-treatment of the chromium layer on top of the silicon substrate can be observed clearly in Figure 4b. A chromium oxide layer, a few nanometres thick, is formed, and the integration between the chromium film and silicon substrate is observable in the APT analysis. The chromium oxide layer enhances the adhesion to the silica and the integration of chromium and silicon contributes to the successful APT analysis of an otherwise challenging multi-layered structure.

## Atom Probe Tomography

An example of an atom probe specimen, imaged using the FIB–SEM post preparation, is shown in Figure 5. Figure 5a presents the specimen imaged using secondary electrons, while 5(b) shows it using backscattered electrons. In Figure 5b, the protective gold cap can be observed at the apex of the tip; to right, a gold nanoparticle can be observed, and beneath it lays the chromia layer. The silica film appears noticeably dark when imaged with backscattered electrons. The silica layer with nanoparticles inside was visible during the lift-out and specimen preparation, making it easier to ensure that the region of interest was included in the final specimen (Supplementary Fig. SI2).

The APT analyses, conducted separately, produced similar results. Typically, a modest number of silica-related ions were detected before ions originating from the gold nanoparticles started to appear, often concurrently with chromia species. Figure 6 shows a reconstructed gold nanoparticle.

Within the nanoparticle shown in Figure 6, silver was found at 1.7% of the amount of gold inside an iso-concentration surface set at 25% gold. The proximity histogram, also known as proxigram, of the isosurface is presented in Figure 6b, showing the silver content to be rather constant in the gold region. During the growth step of the synthesis, silver is added at a 5% molar ratio relative to the gold. Nevertheless, a lower concentration is expected when analyzing the particles as no silver is added to the colloidal solution during the seed particle synthesis. Assuming a spherical seed particle diameter of 10 nm (Supplementary information) and average spherical particle diameter of 30 nm, the silver content is expected to be slightly reduced, roughly 4.8%. The detected amount being lower than the theoretical maximum indicates some loss of silver during the particle synthesis—meaning that not all silver introduced during the growth process ends up in the particles. Moreover, the lower evaporation field of silver compared to gold (Tsong, 1978) may suggest that some silver is lost as preferential evaporation during the analysis.

Due to its dielectric nature, silica exhibits both a relatively high field and high effective k factor (Zhang et al., 2021).

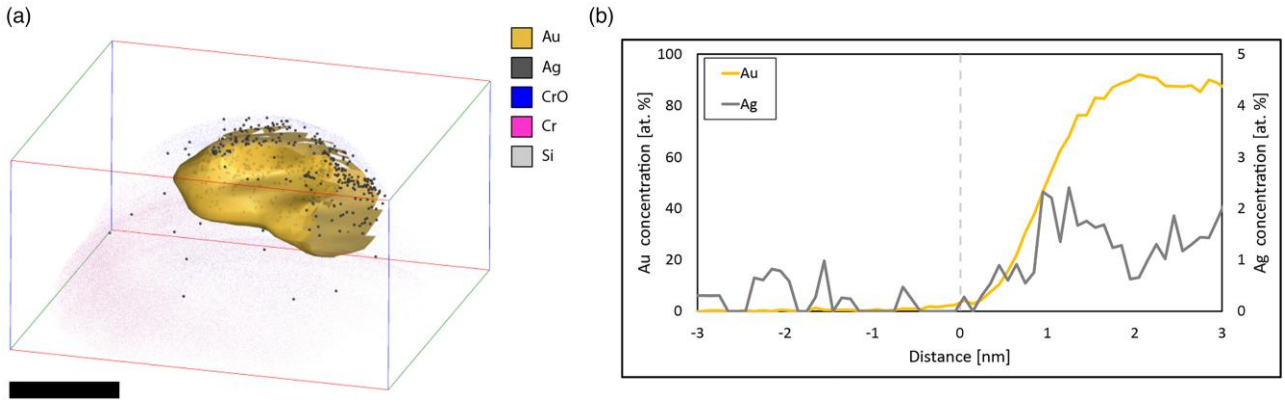


**Fig. 6.** (**a**) APT analysis showing a reconstructed gold nanoparticle embedded in a chromia layer. The isosurface at 25% Au concentration and silver ions are highlighted as spheres. Chromium oxide species are shown in blue and chromium in magenta. Scale bar: 5 nm. (**b**) Proxigram showing the Au and Ag atomic concentrations as a function of the distance to the isosurface in (**a**).

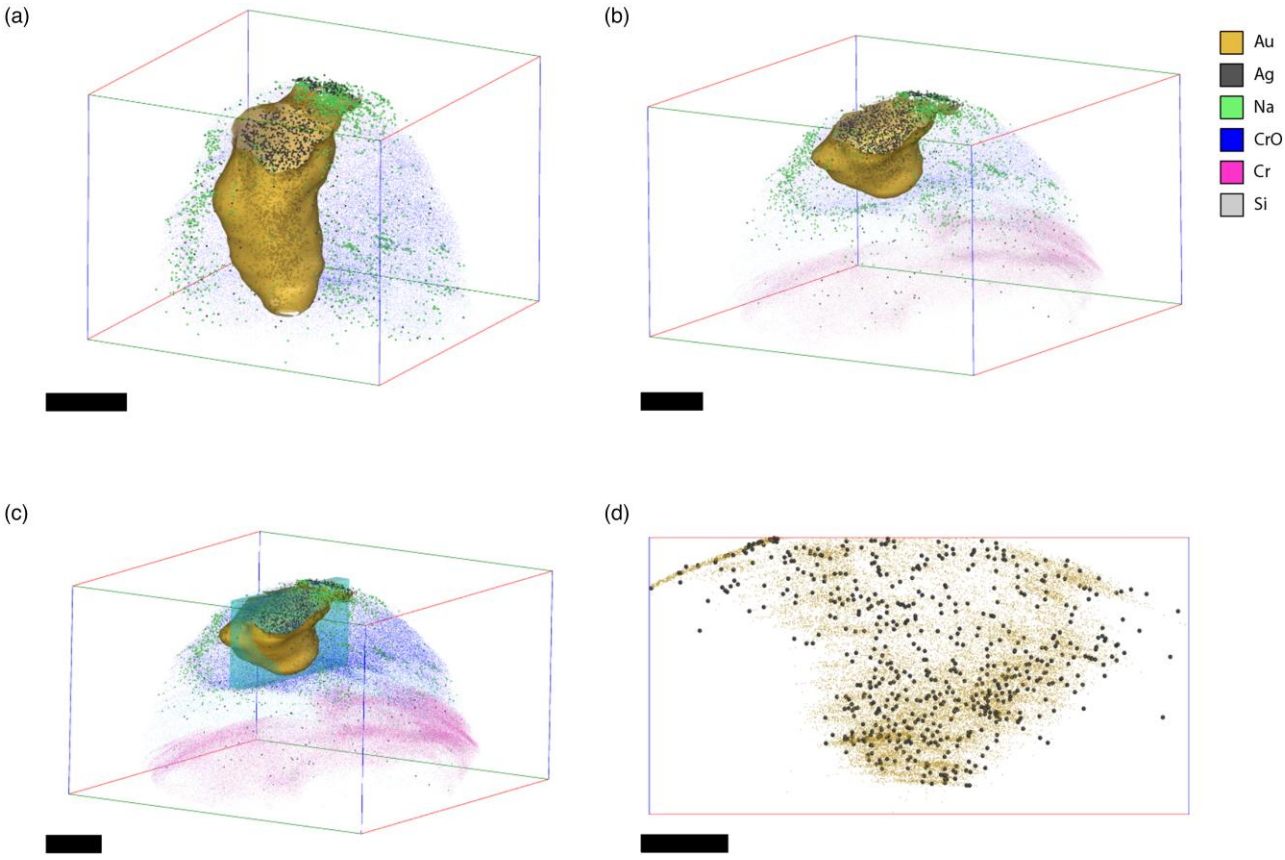


**Fig. 7.** Two reconstructions of the same specimen, carried out with the reconstruction factor *k* set at (**a**) 3.3 and (**b**) 3.0. The isosurfaces are set at 15% gold concentration and the sodium and silver atoms are highlighted as green and dark gray spheres, respectively. In **(c)**, a region of interest volume is introduced to obtain the cross-section shown in **(d)**. The silver content in the particle is clearly visualized. The amount of silver in the region defined by the cross-section is 2.3% relative to the gold. Scale bar: a, b, c: 10 nm. Scale bar: d: 5 nm.

This causes the magnification of silica to be higher, which partly may explain the lack of silica observed in the reconstructions. The field will also be highest at the base of the dielectric silica film, making it a "weak spot" where the specimen is most prone to fracture. While the adhesion between chromia and silica seems to be adequate, ensuring the interface withstands the high voltage requisite for field evaporation, the bond between the gold nanoparticle and silica is presumptively weaker. Consequently, the silica film may delaminate upon the application of a sufficiently high standing voltage, providing another potential explanation for the absence of silica in the analysis. As the silica is absent in all analyses, and the gold nanoparticles appear early on, often after a burst of ions, this is a likely explanation.

In numerous examined reconstructions, similar results were observed as in Figure 7a, where the nanoparticle appeared

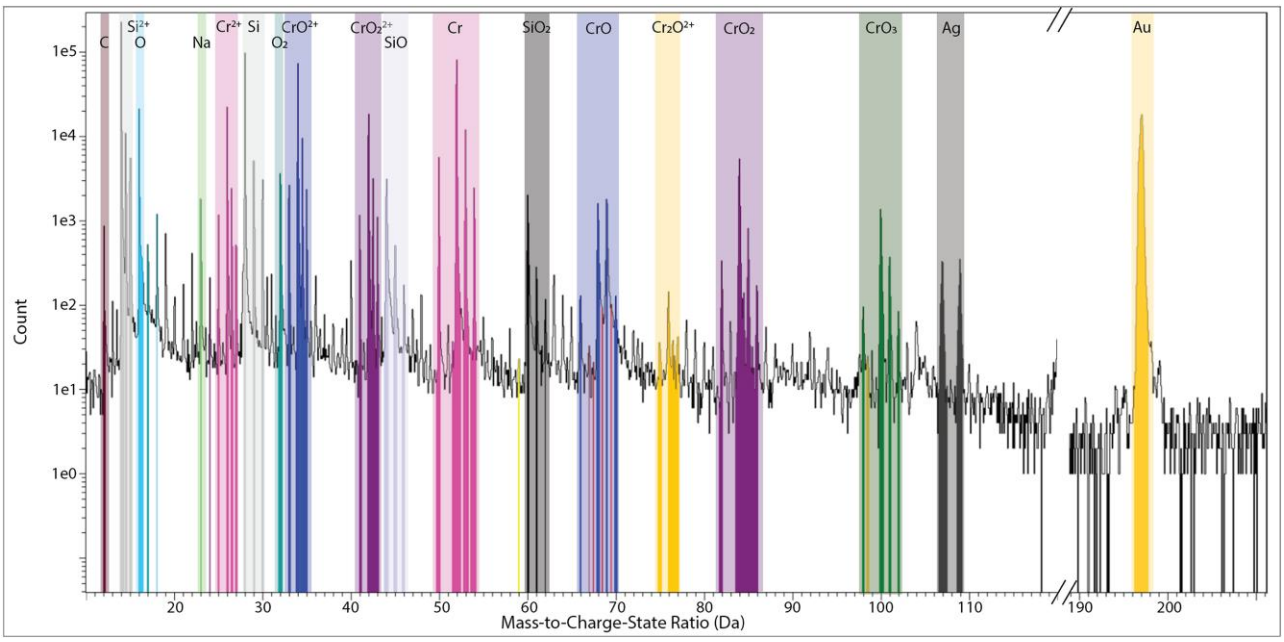


**Fig. 8.** Mass spectrum obtained from the reconstructed specimen in Figure 7. The major peaks are highlighted in the spectrum. Ions without a specified charge are in the first charge state.

distorted and surrounded by species originating from the chromium oxide. The deformed (squeezed) shape of the nanoparticles is reminiscent of previous findings and simulations of particles or precipitates surrounded by a material with a higher evaporation field (Jun et al., 2021). However, by adjusting the reconstruction factor, k, from 3.3 to 3.0, a more spherical particle shape could be achieved, as seen in Figure 7b.

In the reconstructed specimen, sodium, with a mass-to-charge-state ratio at 23 Da ($Na^+$), is observed as clusters on the gold nanoparticles, as seen in Figure 7. A proxigram displaying the sodium surrounding the gold isosurface is found in Supplementary Figure SI4. This observation suggests that the method used for sample preparation may allow for studying ligands or adsorption of stabilizing buffers on the nanoparticles, although the precise origin of the sodium in the present study is uncertain. Sodium is present in the seed particle solution, to stabilize the nanoparticles, as well as in trace amounts in the water glass solution that was spin-coated on the sample surface following the ion exchange.

The silver distribution within the nanoparticles was analyzed by forming a cross-section of the volume shown in Figure 7c, which is visualized in Figure 7d. The gold and silver distribution was found to be somewhat uneven displaying a higher density in the upper left corner of the slice in Figure 7d, probably due to uneven evaporation caused by the varying evaporation fields of the different phases of the specimen, or by the occurrence of microfractures. The silver content in the nanoparticle can also be assessed by a 1D concentration profile, which is shown in Supplementary Figure SI5, together with a density map of the reconstruction.

The suspected delamination of silica, leaving the gold nanoparticle exposed on top of the chromia layer can account for the simultaneous evaporation of chromia and gold, giving the appearance of gold nanoparticles embedded in chromia instead of in silica. This situation would expose chromia, and at sharp edges of this layer, the local field could be sufficiently high to induce field evaporation simultaneous with the evaporation of the gold nanoparticle. Chromia evaporates as a variety of ions, predominantly $CrO^{2+}$, $CrO_2^{2+}$, but also $Cr^{2+}$, $O^+$, $CrO_2^+$, $CrO_3^+$, consistent with previously reported findings (La Fontaine et al., 2015). Further down in the chromia layer, a stochiometric $Si_2Cr$ mixture was identified, likely a result of the heat-treatment of the chromium film during sample preparation. No overlap was observed between the silver at 107–109 Da, gold at 197 Da and ion originating from the matrix. The mass spectrum for the reconstructed specimen in Figure 7 is shown in Figure 8.

APT analysis of nanoparticles can reveal the localization of components and chemical species inside the particles. This is illustrated in a reconstruction of an analyzed gold nanoparticle, that is partly visible and can be seen in Figure 9. The particle is defined by an isosurface set at 25% Au. Inside the defined region, the amount of silver is 4% relative to the gold content, aligning closely with the expected amount based on the particle synthesis protocol.

The silver distribution was evaluated by introducing a cubical ROI as a cross-section of the nanoparticle region, as seen in Figure 9b.

These findings imply that the silver distribution is not homogenous inside the particle, in line with the expected result due to the procedure of the particle synthesis where no silver is used during the synthesis of seed particles, but only added to the growth solution. However, the silver distribution surrounding the seed particle core appears to be homogenous, with the amount of silver on the nanoparticle surface being similar to the concentration in the bulk.

The density of the collected ions is illustrated in Figure 9c and found to be higher in the region corresponding to the gold nanoparticle, compared to the surrounding. This contributes to the smaller than expected size of the nanoparticles (known as local magnification effect), as the magnification is reduced compared to the surrounding material (Vurpillot et al., 2000). Such higher density is normally attributed to a lower evaporation field, and while no definitive claims comparing the evaporation fields in this case are made, the effect can also be explained by several contributing factors.

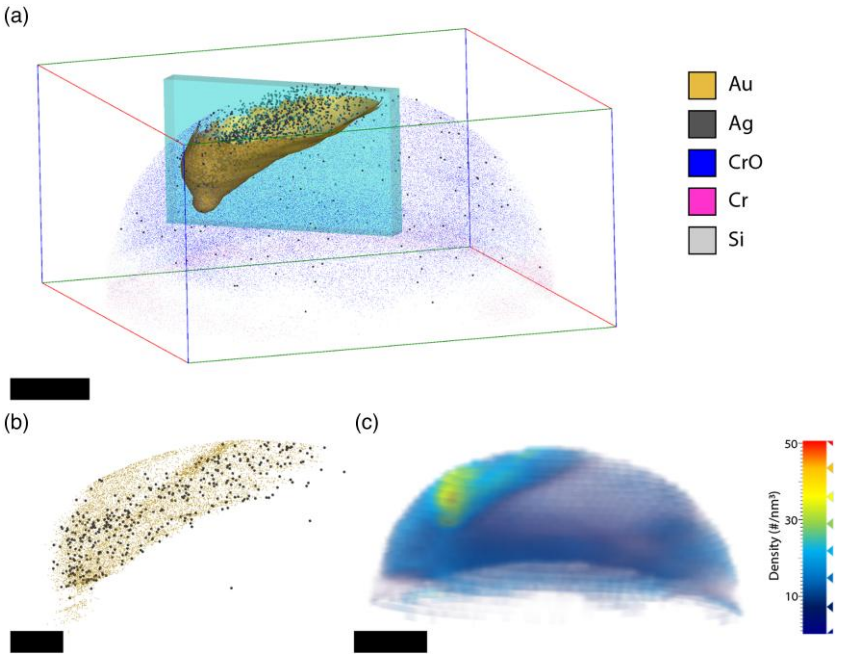


**Fig. 9.** (**a**) Reconstructed Au nanoparticle highlighted by an isosurface set at 25% Au concentration. Silver ions are highlighted as grey spheres. A region of interest is introduced to obtain the cross-section shown in (**b**). Scale bar: 10 nm. (**b**) Gold and silver content of the ROI shown in (**a**). The silver is seen to be concentrated to the lower edge of the gold region. Scale bar: 5 nm. (**c**) Density map of the reconstruction shown in (**a**). Scale bar: 10 nm.

One such factor could be that the green laser is more effectively absorbed by the gold nanoparticles than the chromium oxide, further reducing the evaporation field. Furthermore, it is also possible that the specimen has a nonhemispherical shape due to the suspected microfractures.

In none of the analyzed specimens was an entire gold nanoparticle observed, clearly revealing a core without silver originating from the seed particle surrounded by a silver containing shell from the growth process and containing the number of gold atoms expected from a nanoparticle of the average size observed in Figure 3 (diameter of 30 nm). This is likely due to the challenges related to obtaining an entire particle of this size within a specimen having a diameter below 100 nm and within the limited field of view of the atom probe analysis. While the nanoparticles are small enough to fit inside an APT specimen, considering the measured nearest neighbor distances between the particles and the lack of control over the sharpening of the final specimen at this scale, the probability of a nanoparticle being completely contained and centered in the specimen is relatively low.

The specimens analyzed with the APT instrument equipped with a deep-UV laser produced similar results. During the analysis of the specimen shown in Figure 10, a gold nanoparticle was encountered early in the measurement. As the gold nanoparticle was found just after a spike in the detection rate and consequential drop in the applied voltage (Supplementary Fig. SI6), it likely is related to a microfracture of the silica layer, suggesting that delamination of the silica film occurs when sufficient voltage to achieve field evaporation also in this case. These findings suggest that the inherent challenges when analyzing these materials related to several weak interfaces are not mitigated by utilizing a shorter wavelength laser.

In preceding analyses, the gold nanoparticle appears early on in the measurement together with chromium. The number of gold ions detected in this measurement, adjusted for a 52% detection efficiency, corresponds to a spherical nanoparticle with an approximate diameter of 13 nm. In the obtained data, silver is found evenly distributed inside the nanoparticle at a concentration of 2.4 at% relative to the gold content. The shorter laser wavelength dramatically affects the obtained mass spectrum (Supplementary Fig. SI7), and the mass resolving power is improved. Furthermore, the fraction of multiple events is increased (Supplementary Table SI1). This silver concentration is within the range of the ones measured with the longer laser wavelength, so while effects of the laser wavelength cannot be excluded it does not seem to dramatically alter the measurement. Throughout the measurements, the silver content varies from approximately 2–4 at% of the gold. While some effects from experimental conditions, such as laser wavelength, on the measured composition cannot be excluded, it is likely that this also illustrates the variation in silver content between individual particles synthesized by a colloidal seed–growth protocol.

Sodium is detected surrounding the nanoparticle in a similar fashion to the previous measurements. Interestingly, carbon is also detected in the vicinity of the sodium, suggesting that the stabilizing sodium citrate ligands on the nanoparticles are observed. The presence of these elements surrounding the particle is illustrated by a proxigram in Figure 10b. However, it should be noted that other sources of sodium and carbon are possible, as sodium is found in the silica precursor used and carbon contaminations from other sources during sample preparation is possible. APT analyses of the silica as bulk material shows that sodium and carbon is also found there. However, as the silica film consistently delaminate from the specimens during analysis, it can be suspected that sodium and carbon present in the silica is lost as well and do not influence the analysis. Since no Pt was detected, it is unlikely that the carbon is originating from the FIB/SEM process. For further confidence when investigating sodium containing capping ligands on nanoparticles in particular, the methodology can be

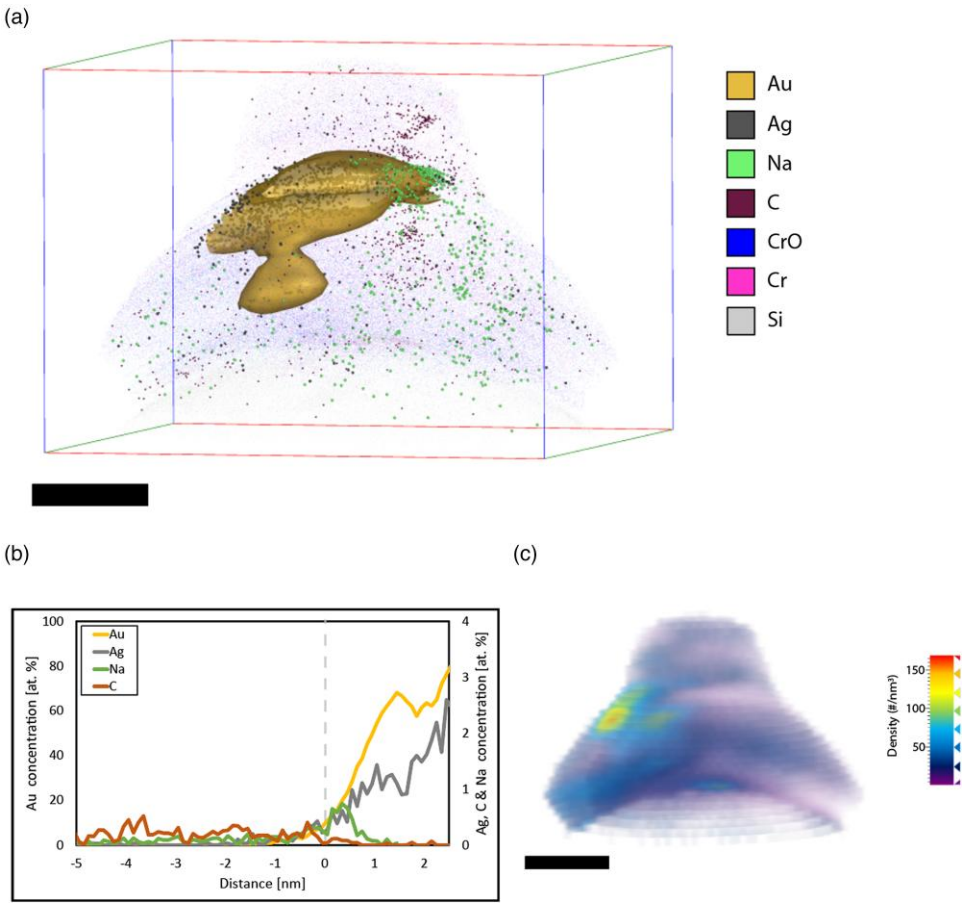


**Fig. 10.** (**a**) Reconstruction of gold nanoparticle obtained by deep-UV laser assisted APT. Gold is highlighted using a 25% isosurface. Silver, sodium, and carbon are highlighted as spheres. Scale bar: 10 nm. (**b**) Proxigram displaying the silver, sodium, and carbon atomic concentrations surrounding the gold isosurface in the reconstruction shown in (**a**). (**c**) Density map of the reconstruction shown in (**a**). Scale bar: 10 nm.

further developed to use other silica precursors such as potassium silicates. Nonetheless, these results elucidate the potential to examine ligands on nanoparticles. The density map in Figure 10c shows consistent behavior with the ones obtained in previous analyses, where the density is higher in the region corresponding to the gold nanoparticle than in the surroundings. While other embedding techniques, such as sputter- or ALD-coating, can give a higher success rate in analyzing the interface between the matrix and nanoparticles, these methods risk altering or damaging the particle's surfaces and ligands.

The results presented here demonstrate that the methodology allows for efficient analysis of these types of nanoparticles. The packing of the nanoparticles on the substrate surface provides a high probability of encountering a particle within an analyzed specimen; however, considering the size of the particles compared to the radius of an APT specimen, it is likely that only parts of the particle will be captured within the analyzed volume. The silica embedding of the particles indicates that it can be possible to retain the ligands on the nanoparticles. The presented procedure could be utilized to study other nanostructured liquid–solid interfaces by replacing the water with a silica matrix, allowing for cryo-free specimen preparation of such features that are notoriously difficult to characterize.

In the samples where proteins were attempted to be attached to the nanoparticles prior to silica embedding, sodium, but no proteins were detected. However, in these analyses, the origin of sodium can also be attributed to the protein buffer solution. Should the method evolve to enable the binding of biomolecules, like proteins, to the nanoparticles that are preserved postsilica embedding, it may present a meaningful addition to the progressive efforts to devise methods for studying biomolecules in their inherent hydrated state using APT.

## Conclusions

Herein, we have demonstrated a method for sample preparation for APT, enabling the systematic study of nanoparticles with a substantial proportion of the analyzed specimen incorporating the particles under investigation. The methodology reveals the potential to attain valuable information, such as the internal chemical composition regarding concentration and distribution of solutes with high sensitivity and resolution. Limitations of the method seem to be that multilayer structure with varying fields can cause aberrations in the reconstruction, making the nanoparticles appear distorted. Additionally, depending on the surface chemistry of the nanoparticles, poor adhesion between the silica and the particle may cause the silica to fracture under the high field induced stress. Despite these challenges, they appear noncritical for the ongoing analysis of the specimen.

Observations of sodium-enriched regions on the nanoparticle surfaces, potentially deriving from the stabilizing sodium citrate ligands utilized during particle synthesis, open ways for not only studying the nanoparticles but also examining their surface ligands in a hydrated state. Furthermore, the

methodology could be applied to study other liquid–solid interfaces, potentially including ones decorated with biomolecules.

## Acknowledgments

This work was performed in part at the Chalmers Material Analysis Laboratory, CMAL.

## Availability of Data and Materials

Data available upon request.

## Supplementary Material

To view supplementary material for this article, please visit https://doi.org/10.1093/mam/ozae024.

## Financial Support

This work was funded by the Knut and Alice Wallenberg Foundation, KAW, as well as the European Union, under Horizon Europe Programme (grant agreement 101046651—MIMOSA).

## Conflict of Interest

The authors declare that they have no competing interest.

## References

Bhatia RB, Brinker CJ, Gupta AK & Singh AK (2000). Aqueous sol-gel process for protein encapsulation. *Chem Mater* **12**, 2434–2441. https://doi.org/10.1021/cm000260f

De M, Ghosh PS & Rotello VM (2008). Applications of nanoparticles in biology. *Adv Mater* **20**, 4225–4241. https://doi.org/10.1002/adma.200703183

Ealias AM & Saravanakumar MP (2017). A review on the classification, characterisation, synthesis of nanoparticles and their application. *IOP Conf Ser: Mater Sci Eng* **263**, 032019. https://doi.org/10.1088/1757-899X/263/3/032019

Felfer P, Benndorf P, Masters A, Maschmeyer T & Cairney JM (2014). Revealing the distribution of the atoms within individual bimetallic catalyst nanoparticles. *Angewandte Chem—Int Edn* **53**, 11190–11193. https://doi.org/10.1002/anie.201405043

Felfer P, Li T, Eder K, Galinski H, Magyar AP, Bell DC, Smith GDW, Kruse N, Ringer SP & Cairney JM (2015). New approaches to nanoparticle sample fabrication for atom probe tomography. *Ultramicroscopy* **159**, 413–419. https://doi.org/10.1016/j.ultramic.2015.04.014

Gault B, Chiaramonti A, Cojocaru-Mirédin O, Stender P, Dubosq R, Freysoldt C, Makineni SK, Li T, Moody M & Cairney JM (2021). Atom probe tomography. *Nat Rev Methods Primers* **1**, 51. https://doi.org/10.1038/s43586-021-00047-w

Goia DV & Matijević E (1998). Preparation of monodispersed metal particles. *New J Chem* **22**, 1203–1215. https://doi.org/10.1039/a709236i

Hernández-Saz J, Herrera M & Molina SI (2012). A methodology for the fabrication by FIB of needle-shape specimens around sub-surface features at the nanometre scale. *Micron* **43**, 643–650. https://doi.org/10.1016/j.micron.2011.11.011

Jang K, Kim SH, Jun H, Jung C, Yu J, Lee S & Choi PP (2021). Three-dimensional atomic mapping of ligands on palladium nanoparticles by atom probe tomography. *Nat Commun* **12**, 4301. https://doi.org/10.1038/s41467-021-24620-9

Joo SH, Park JY, Tsung CK, Yamada Y, Yang P & Somorjai GA (2009). Thermally stable pt/mesoporous silica core-shell nanocatalysts for high-temperature reactions. *Nat Mater* **8**, 126–131. https://doi.org/10.1038/nmat2329

Jun H, Jang K, Jung C & Choi PP (2021). Atom probe tomography investigations of Ag nanoparticles embedded in pulse-electrodeposited Ni films. *Microsc Microanal* **27**, 1007–1016. https://doi.org/10.1017/S1431927621012137

Kim S-H, El-Zoka AA & Gault B (2021). A liquid metal encapsulation for analyzing porous nanomaterials by atom probe tomography. *Microsc Microanal*, **28**, 1198–1206. https://doi.org/10.1017/S1431927621012964

Kim SH, Jang K, Kang PW, Ahn JP, Seol JB, Kwak CM, Hatzoglou C, Vurpillot F & Choi PP (2020). Characterization of Pd and Pd@Au core-shell nanoparticles using atom probe tomography and field evaporation simulation. *J Alloys Compd* **831**, 154721. https://doi.org/10.1016/j.jallcom.2020.154721

La Fontaine A, Yen HW, Felfer PJ, Ringer SP & Cairney JM (2015). Atom probe study of chromium oxide spinels formed during intergranular corrosion. *Scr Mater* **99**, 1–4. https://doi.org/10.1016/j.scriptamat.2014.09.028

Mahl D, Diendorf J, Ristig S, Greulich C, Li ZA, Farle M, Köller M & Epple M (2012). Silver, gold, and alloyed silver-gold nanoparticles: Characterization and comparative cell-biologic action. *J Nanopart Res* **14**, 1–13. https://doi.org/10.1007/s11051-012-1153-5

Miller MK, Longstreth-Spoor L & Kelton KF (2011). Detecting density variations and nanovoids. *Ultramicroscopy* **111**, 469–472. https://doi.org/10.1016/j.ultramic.2011.01.027

Mosiman DS, Chen YS, Yang L, Hawkett B, Ringer SP, Mariñas BJ & Cairney JM (2021). Atom probe tomography of encapsulated hydroxyapatite nanoparticles. *Small Methods* **5**, 2000692. https://doi.org/10.1002/smtd.202000692

Mourdikoudis S, Pallares RM & Thanh NTK (2018). Characterization techniques for nanoparticles: Comparison and complementarity upon studying nanoparticle properties. *Nanoscale* **10**, 12871–-12934. https://doi.org/10.1039/C8NR02278J

Novi Inverardi G, Carnovale F, Petrolli L, Taioli S & Lattanzi G (2023). Silica in silico: A molecular dynamics characterization of the early stages of protein embedding for atom probe tomography. *Biophysica* **3**, 276–287. https://doi.org/10.3390/biophysica3020018

Park YK & Park S (2008). Directing close-packing of midnanosized gold nanoparticles at a water/hexane interface. *Chem Mater* **20**, 2388–2393. https://doi.org/10.1021/cm703498y

Personick ML, Langille MR, Zhang J & Mirkin CA (2011). Shape control of gold nanoparticles by silver underpotential deposition. *Nano Lett* **11**, 3394–3398. https://doi.org/10.1021/nl201796s

Qiu S, Zheng C, Zhou Q, Dong D, Shi Q, Garg V, Cheng W, Marceau RKW, Sha G & Fu J (2020). Direct imaging of liquid-nanoparticle interfaces with atom probe tomography. *J Phys Chem C* **124**, 19389–19395. https://doi.org/10.1021/acs.jpcc.0c05504

Rajput N (2015). Methods of preparation of nanoparticles-a review. *Int J Adv Eng Technol* **7**, 1806–1811.

Reddy SM, Saxey DW, Rickard WDA, Fougerouse D, Montalvo SD, Verberne R & van Riessen A (2020). Atom probe tomography: Development and application to the geosciences. *Geostandards Geoanal Res* **44**, 5–50. https://doi.org/10.1111/ggr.12313

Rioux D & Meunier M (2015). Seeded growth synthesis of composition and size-controlled gold-silver alloy nanoparticles. *J Phys Chem C* **119**, 13160–13168. https://doi.org/10.1021/acs.jpcc.5b02728

Stark WJ, Stoessel PR, Wohlleben W & Hafner A (2015). Industrial applications of nanoparticles. *Chem Soc Rev* **44**, 5793–5805. https://doi.org/10.1039/C4CS00362D

Sundell G, Hulander M, Pihl A & Andersson M (2019). Atom probe tomography for 3D structural and chemical analysis of individual proteins. *Small* **15**, 1900316. https://doi.org/10.1002/smll.201900316

Thompson K, Lawrence D, Larson DJ, Olson JD, Kelly TF & Gorman B (2007). In situ site-specific specimen preparation for atom probe tomography. *Ultramicroscopy* **107**, 131–139. https://doi.org/10.1016/j.ultramic.2006.06.008

Tsong TT (1978). Field ion image formation. *Surf Sci* **70**, 211–233. https://doi.org/10.1016/0039-6028(78)90410-7

Vurpillot F, Bostel A & Blavette D (2000). Trajectory overlaps and local magnification in three-dimensional atom probe. *Appl Phys Lett* **76**, 3127–3129. https://doi.org/10.1063/1.126545

Wang X, Hatzoglou C, Sneed B, Fan Z, Guo W, Jin K, Chen D, Bei H, Wang Y, Weber WJ, Zhang Y, Gault B, More KL, Vurpillot F & Poplawsky JD (2020). Interpreting nanovoids in atom probe tomography data for accurate local compositional measurements. *Nat Commun* **11**, 1–11. https://doi.org/10.1038/s41467-020-14832-w

Zhang Q, Klein B, Sanford NA & Chiaramonti AN (2021). Comparative apex electrostatics of atom probe tomography specimens. *J Electron Mater* **50**, 3022–3029. https://doi.org/10.1007/s11664-021-08932-6.

TESCAN
PERFORMANCE IN NANOSPACE

# TESCAN FIB-SEM

Drive your materials development
and get comprehensive answers.

**Fast and effortless!**

**info.tescan.com/matsci-fib-sem**

Scan for more information